ELSEVIER

International Journal of Heat and Fluid Flow 23 (2002) 823–830

International Journal of HEAT AND FLUID FLOW

www.elsevier.com/locate/ijhff

Buoyancy-induced flow and convective heat transfer in an inclined arc-shape enclosure

Chin-Lung Chen, Chin-Hsiang Cheng *

Department of Mechanical Engineering, Tatung University, 40 Chungshan N. Road, Sec. 3, Taipei 10451, Taiwan, ROC

Received 1 June 2001; accepted 8 March 2002

Abstract

Numerical and experimental investigations have been conducted to study the flow and heat transfer characteristics for the buoyancy-induced flow inside an inclined arc-shape enclosure. Mathematical model in form of a stream function-vorticity formulation representing the laws of conservation in mass, momentum, and energy is expressed in a curvilinear coordinate frame and solved by a finite-volume discretization method. Heat transfer and flow pattern are predicted at various Grashof numbers and inclination angles. Meanwhile, an experimental system is developed and a flow-visualization technique using smoke is employed to observe the flow pattern. Results show that only when the Grashof number is higher than 10^5, the increase in natural convection heat transfer becomes appreciable. Both the strength and the pattern of the buoyancy-induced vortex are found to be greatly dependent on the inclination angle. The range of the Grashof number considered in this study is up to 10^7 and the inclination angle is varied from 0 to π.

1. Introduction

The understanding for the flow behavior within an irregular enclosure is recently regarded as one of the fundamental concerns to the researchers of fluid-dynamics and hence, the problems have been pursued extensively. As a matter of fact, a number of studies dealing with different kinds of enclosures have been performed and the solutions for both the flow and thermal fields have been presented. However, most of the previous studies, for example, Ghia et al. (1982) and Theodossiou and Sousa (1986), were focused on the analysis of the fluid motion in a rectangular enclosure, and a relatively smaller number of reports considered the enclosure with an irregular shape. To name a few reports concerning the irregular enclosures, Lee et al. (1992) studied natural convention in the enclosures with irregular walls and reviewed the schemes useful for numerical predictions. Cheng and Chao (1996) investigated the buoyancy-driven flow in the annulus between two horizontal eccentric elliptical cylinders.

Recently, Chang and Cheng (1999) presented numerical solutions for a lid-driven flow in an arc-shape cavity. However, in their report, no experimental data have been provided to demonstrate the numerical predictions obtained. Investigation of natural convection in an enclosure of arc-shape cross-section is of great relevance to a number of engineering applications, such as concentrating solar collectors (Farouk Kothdiwala et al., 1995), lubrication systems (Payver, 1991; Berger et al., 1996) and air-conditioning devices. Overall heat transfer performance for these devices is greatly dependent on the flow behavior and heat convection inside the enclosures. Despite of this, the heat convention in an arc-shape enclosure has not been sufficiently investigated.

On the other hand, according to the reports presented by a number of authors (Khanafer and Chamkha, 1998; Lai and Lu, 1996; Hartley et al., 1999; Cheng and Yu, 1999), it is recognized that the inclination angle of an enclosure has profound influence on the natural convection heat transfer in that enclosure. Therefore, one readily expects that the inclination may also play an important role in the arc-shape enclosures. To the authors' knowledge, both the numerical and the experimental data pertinent to the inclination effects on the flow in an arc-shape enclosure are still not available.

* Corresponding author. Tel.: +886-02-25925252-3410; fax: +886-02-25997142.

E-mail address: cheng@ttu.edu.tw (C.-H. Cheng).

0142-727X/02/$ - see front matter © 2002 Published by Elsevier Science Inc.
PII: S0142-727X(02)00189-3

Nomenclature

L	width of enclosure
g	gravitational acceleration
Gr	Grashof number
h	heat transfer coefficient
J	Jacobian of coordinate transformation
k	thermal conductivity
Nu_x	local Nusselt number
Nu	overall Nusselt number
Pr	Prandtl number
r	radius
Re	Reynolds number
$\overline{T}$	dimensionless temperature
T_L	lower temperature at flat wall
T_H	higher temperature at arc-shape wall
u,v	velocity components in x- and y-directions
U,V	dimensionless velocity components in x- and y-directions
x,y	rectangular coordinates
X,Y	dimensionless rectangular coordinates

Greeks

θ	inclination angle
$\bar{\alpha}$	thermal diffusivity of fluid
$\bar{\beta}$	coefficient of volumetric expansion of fluid
α,β,γ	coordinate transformation coefficients
ν	kinematic viscosity of fluid
ξ,η	body-fitted curvilinear coordinate
ϕ	stream function
ψ	dimensionless stream function
ω	vorticity
Ω	dimensionless vorticity

In these circumstances, the aim of this paper is to perform numerical study of the buoyancy-induced flow motion and heat convection in an inclined arc-shape enclosure. Meanwhile, a flow visualization technique is employed to observe the flow pattern. Comparison between the numerical predictions and the visualized flow patterns can thus be provided. The physical model of this problem is shown in Fig. 1(a). An inclined enclosure of width L and with inclination angle θ is confined between an arc-shape wall and a flat wall. The flat wall is maintained at a lower temperature (T_L), and the arc-shape wall is maintained at a higher temperature (T_H). The arc profile is defined by the expression $(x-p)^2+(y-q)^2=r^2$, which denotes a circle of radius r with the center located at point (p,q). In this study, the ratios $p/r, q/r$, and r/L are fixed at $1/2, 1/2\sqrt{3}$, and $1/\sqrt{3}$, respectively.

Two major dimensionless parameters are varied in the analysis. The Grashof number (Gr) is varied within the range $10^4 \leqslant Gr \leqslant 10^7$, and the inclination angle (θ) is in the range $0 \leqslant \theta \leqslant \pi$. The Prandtl ($Pr$) number is assigned to be 0.7 for air.

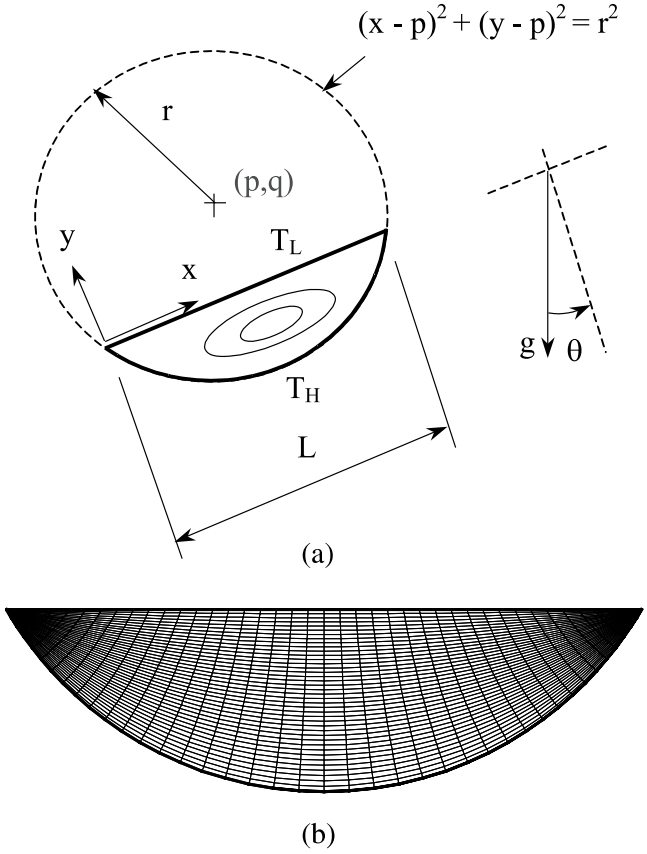

Fig. 1. An inclined arc-shape enclosure. (a) physical model, (b) grid system.

2. Theoretical analysis

The fluid properties are assumed constant except for the variation of density in the buoyancy terms of the momentum equations, which is approximated by the Boussinesq assumption. Meanwhile, the flow field is considered to be steady, laminar, and two-dimensional. The dimensionless stream function-vorticity formulation representing the laws of conservation in mass, momentum, and energy can be expressed in curvilinear coordinate as

$$\alpha\Psi_{\eta\eta} - 2\beta\Psi_{\xi\eta} + \gamma\Psi_{\xi\xi} = -J^2\Omega \tag{1}$$

$$J\Psi_\eta\Omega_\xi - J\Psi_\xi\Omega_\eta = \left(\alpha\Omega_{\eta\eta} - 2\beta\Omega_{\xi\eta} + \gamma\Omega_{\xi\xi}\right) + JGr\left[\cos\theta\left(Y_\eta\overline{T}_\xi - Y_\xi\overline{T}_\eta\right) - \sin\theta\left(X_\xi\overline{T}_\eta - X_\eta\overline{T}_\xi\right)\right] \tag{2}$$

$$JPr\Psi_\eta\overline{T}_\xi - JPr\Psi_\xi\overline{T}_\eta = \alpha\overline{T}_{\eta\eta} - 2\beta\overline{T}_{\xi\eta} + \gamma\overline{T}_{\xi\xi} \tag{3}$$

$$U = \frac{1}{J}\left(-X_\eta\Psi_\xi + X_\xi\Psi_\eta\right) \tag{4}$$

$$V = \frac{1}{J}\left(-Y_\eta\Psi_\xi + Y_\xi\Psi_\eta\right) \tag{5}$$

$$\Omega = \frac{1}{J}\left[\left(Y_\eta V_\xi - Y_\xi V_\eta\right) + \left(X_\eta U_\xi - X_\xi U_\eta\right)\right] \tag{6}$$

where

$$\begin{aligned}\alpha &= X_\eta^2 + Y_\eta^2\\ \beta &= X_\xi X_\eta + Y_\eta Y_\xi\\ \gamma &= X_\xi^2 + Y_\xi^2\\ J &= X_\eta Y_\xi - X_\xi Y_\eta\end{aligned} \tag{7}$$

Note that J denotes the Jacobian of the coordinate mapping from the rectangular coordinates (X, Y) to the curvilinear coordinates (ξ, η). These dimensionless variables are define by

$$\begin{aligned}&X = \frac{x}{L},\quad Y = \frac{y}{L},\quad U = \frac{u}{\nu/L},\quad V = \frac{v}{\nu/L},\\ &\Psi = \frac{\phi}{\nu},\quad \Omega = \frac{\omega L^2}{\nu},\quad \overline{T} = \frac{T - T_L}{T_H - T_L},\quad Pr = \frac{\nu}{\bar{\alpha}},\\ &Gr = \frac{g\bar{\beta}(T_H - T_L)L^3}{\nu^2}\end{aligned} \tag{8}$$

Boundary conditions associated with the above governing equations are given by

$$\begin{aligned}&\text{On flat wall: } U = 0,\ V = 0,\ \overline{T} = 0,\\ &\quad \Psi = 0,\ \text{and } \Omega = -\frac{X_\xi}{J}U_\eta\\ &\text{On arc-shape wall: } U = 0,\ V = 0,\ \overline{T} = 1,\\ &\quad \Psi = 0,\ \text{and } \Omega = -\frac{1}{J}\left(Y_\xi V_\eta + X_\xi U_\eta\right)\end{aligned} \tag{9}$$

3. Numerical methods

The coordinate transformation functions $\xi = \xi(X, Y)$ and $\eta = \eta(X, Y)$ denoting the curvilinear coordinate system are obtained by using similar methods as those described by Cheng and coworkers (Cheng and Chao, 1996; Cheng and Yu, 1999). Eqs. (1)–(9), are then discretized and solved by using the finite-volume method in the curvilinear coordinates (ξ, η). Fig. 1(b) displays the curvilinear grid system employed in this study. In the present problem, the local heat transfer rate near the two corners of the enclosure is extremely high and thus strongly dependent on the sizes and arrangement of the grid system. Therefore, the grid sizes should be sufficiently small to ensure accuracy of the computation. It can be observed that the curvilinear grid system shown in Fig. 1(b) essentially has much finer grid sizes near the two corners, and therefore, it is particularly suitable for the present problem. Note that each of the two corners at $x/L = 0$ and 1.0 of the arc-shape physical domain is actually transformed into a face of a rectangular computation domain during curvilinear coordinate transformation. In this manner, each corner is represented by a series of grid points distributed on the face. For dealing with the singularity of dimensionless temperature ($\overline{T}$) at the corners, the boundary conditions of the dimensionless temperature is assumed to be linearly varied from $\overline{T} = 0$ to 1 at the grid points on the respective faces.

A grid system of 101×101 grid points for the solution domain is adopted typically in the analysis. However, a careful check for the grid independence of the numerical solution has been made to ensure the accuracy and validity of the numerical schemes. For this purpose, three grid systems, 41×41, 81×81, and 101×101 are tested. For two particular cases, Fig. 2 shows the comparison in flow patterns based on these three grid systems. Results show that for the cases at (a) $Gr = 10^4$ and $\theta = \pi/4$ and (b) $Gr = 10^6$ and $\theta = \pi/2$, the relative error in the maximum values of stream function in the enclosure obtained through the three grid systems is no more than 2%.

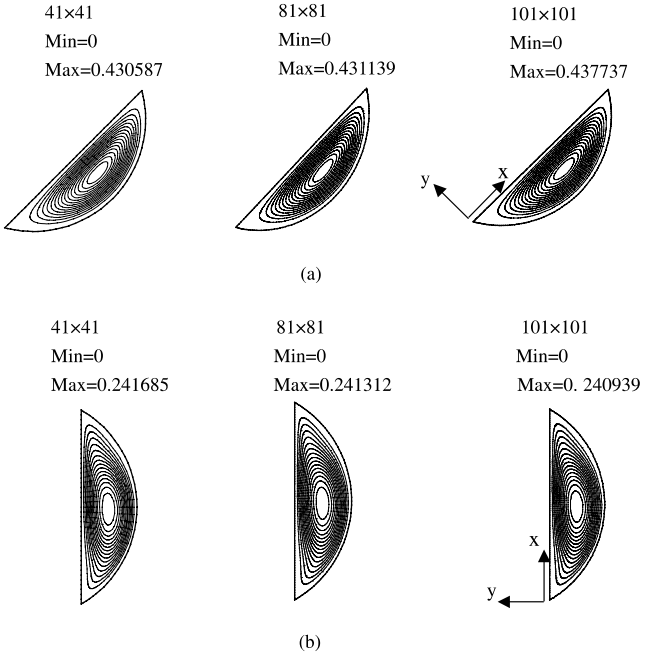

Fig. 2. Grid-independence check with flow patterns for two cases based on three different grids: (a) $Gr = 10^4$, $\theta = \pi/4$, (b) $Gr = 10^6$, $\theta = \pi/2$.

4. Flow visualization apparatus and methods

The layout of the flow visualization apparatus and the dimensions of the tested enclosure are shown in Fig. 3. The length and the width of the enclosure are 210 and 30 mm, respectively, with a length-to-diameter ratio of 7. A copper tube with a thickness of 3 mm is cut into two parts, and the smaller part is specified such that it forms the arc-shape bottom wall of the enclosure. The arc-shape bottom wall is heated by an electric resistance heater until a sufficiently high temperature is reached. The electric heater is designed to comply with the profile of the bottom wall. Temperatures of the bottom and the flat walls (T_H and T_L) are measured by K-type thermocouples and are recorded by a data acquisition system for later data analysis.

Numerical methods have been developed for flow visualization. Smoke flow visualization is one of the most widely used techniques for the natural convective air flows. In this study, the smoke is produced by a similar method employed by Cheng et al. (1997). The smoke is fed to the enclosure through a smoke rake placed beneath the arc-shape bottom wall. The photographs of the visualized flow patterns are taken by using a camera and a light unit installed outside the test section. In the experiment, all the properties of the fluid are evaluated at the film temperature.

5. Results and discussion

5.1. Flow and temperature distributions

Results of flow field and temperature distribution are displayed in this section with streamlines and isotherms, respectively. Effects of Grashof number on the flow pattern and temperature distribution at $\theta = 0$ are shown in Fig. 4. Flow patterns for various Grashof numbers are plotted in the left half of this figure by using streamlines, and the isotherms are displayed in the right half to illustrate the temperature distributions. In each plot, maximum and minimum values of the quantities are provided for a quantitative comparison. It is clearly observed that the strength of the buoyancy-induced

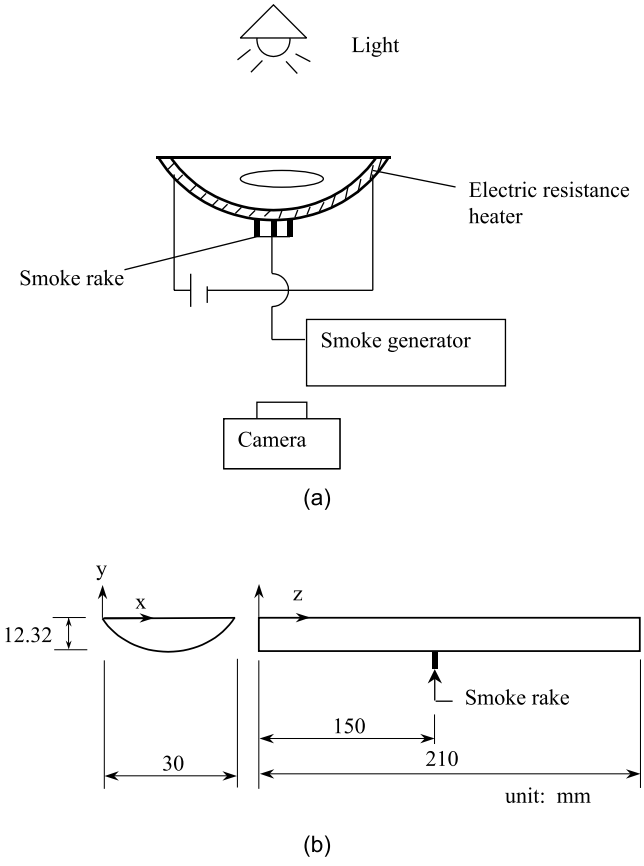

Fig. 3. Flow visualization apparatus: (a) layout of experimental apparatus, (b) dimensions of tested enclosure.

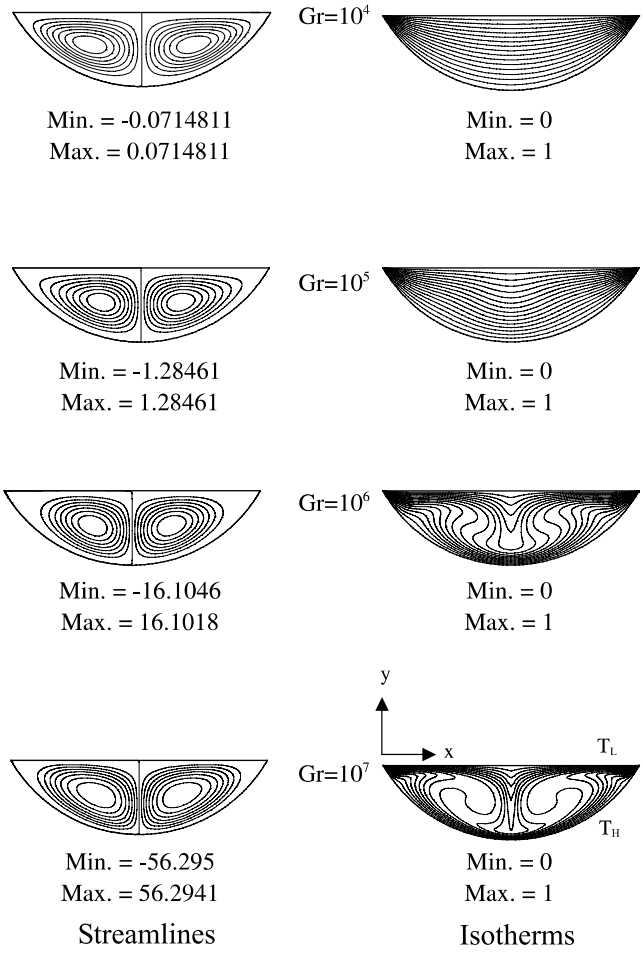

Fig. 4. Effect of Grashof number on the flow pattern and temperature distribution at $\theta = 0$.

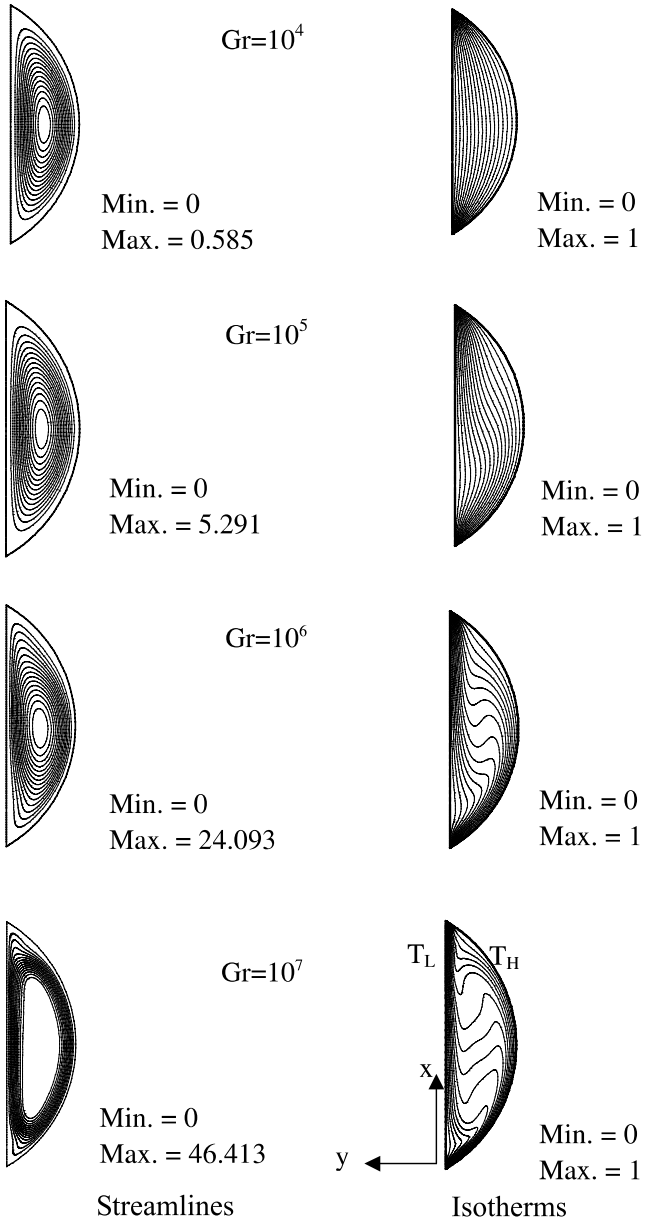

Fig. 5. Effects of Grashof number on the flow pattern and temperature distribution at $\theta = \pi/2$.

vortices increases with Gr and that a flow pattern of two symmetric cells is found within $10^4 \leqslant Gr \leqslant 10^7$ for $\theta = 0$.

Fig. 5 shows the flow patterns and temperature distributions at various Grashof numbers for an inclined enclosure with $\theta = \pi/2$. It is observed that at this inclination angle the flow field features a one-cell pattern and a thermal boundary layer is formed along the flat wall.

Presented in Fig. 6 are the numerical results for the case at $\theta = \pi$. Note that the case at $\theta = \pi$ represents a top-heating situation, in which a thermal stratification prevails in the entire solution domain. As a result, the strength of the symmetric vortices is relatively weak in comparison with the case at $\theta = 0$ shown in Fig. 4. This also leads to weaker heat convection in the enclosure.

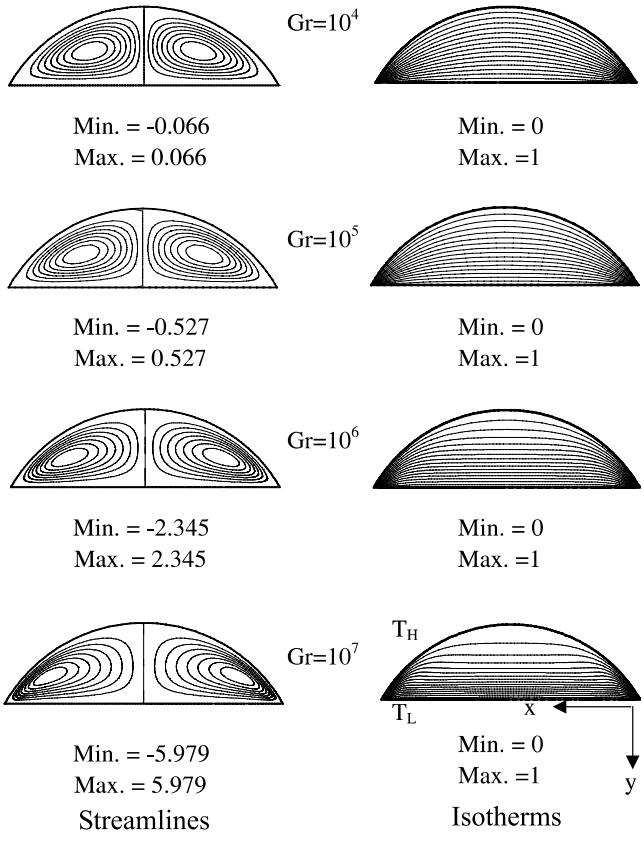

Fig. 6. Effects of Grashof number on the flow pattern and temperature distribution at $\theta = \pi$.

5.2. Comparison between numerical and experimental data

The numerical predictions of the flow patterns have been verified with the flow visualization photographs. Fig. 7(a) conveys the numerical predictions of the effects of the inclination angle on the flow pattern at $Gr = 10^5$, and the photographs showing the flow patterns for different inclination angles at the same Grashof number are given in Fig. 7(b). Variation in the vortex structure with the inclination angle can be clearly observed. The vortex strength and pattern are found to be dependent on the inclination angle. At $\theta = 0$ or π, a flow pattern of two symmetric cells is seen, whereas at other inclination angles the flow field features a one-cell pattern. Fluid velocity and the strength of the vortex cannot be provided simply based on the photographs of flow visualization. However, inspite of this, the agreement between the numerical and the experimental results is fairly good.

Based on the experimental information gathered by using the flow visualization apparatus in this study, the flow remains two-dimensional for various inclination angles as $Gr \leqslant 10^6$. Unfortunately, owing to the capacity limit of the experimental system, no experimental observation is performed at a higher Grashof number. For

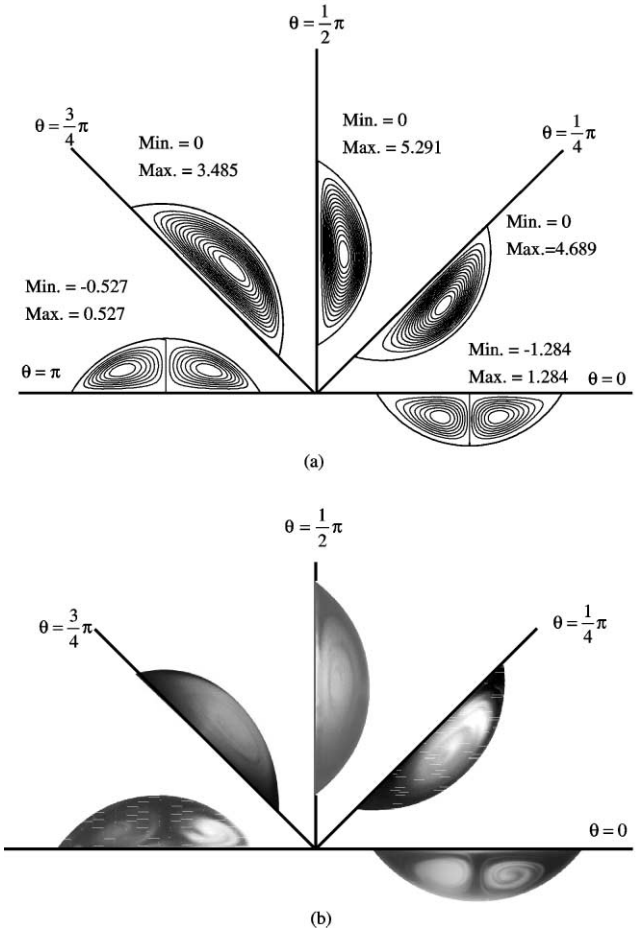

Fig. 7. Effects of inclination angle on the flow pattern at $Gr = 10^5$: a comparison between numerical and experimental data: (a) numerical predictions, (b) flow visualization photographs.

the case at $\theta = 0$, the flow becomes thermally unstable because of a bottom-heating situation. This may result in a three-dimensional flow, especially when the Grashof number is high. Further experimental studies are definitely required to clarify the interesting three-dimensional unstable flow behavior.

5.3. Heat transfer

The solutions for temperature distribution enable the local Nusselt numbers on the two walls to be further evaluated. Local Nusselt number on the flat wall is defined by

$$Nu_x = \frac{h_x L}{k} = \frac{L}{T_H - T_L} \left.\frac{\partial T}{\partial n}\right|_{flat} \tag{10}$$

where h_x is the local heat transfer coefficient defined by

$$h_x(T_H - T_L) = k \left.\frac{\partial T}{\partial n}\right|_{flat} \tag{11}$$

and n is the outward normal coordinate to the flat wall.

Based on the results of the local Nusselt number, the overall Nusselt number on the wall can then be evaluated by integration as

$$Nu = \int_0^1 Nu_x \, dX \tag{12}$$

Note that the magnitudes of the overall Nusselt numbers are equal on the flat and the arc-shape walls due to the conservation in energy transfer.

The overall Nusselt number as a function of Gr and θ is shown in Figs. 8 and 9. Presented in Fig. 8 are the results of Nu versus θ for various Grashof numbers. It is clearly found that Nu increases with Gr and that the value of Nu attains a minimum at $\theta = \pi$. The poor heat transfer performance at $\theta = \pi$ may be attributed to the

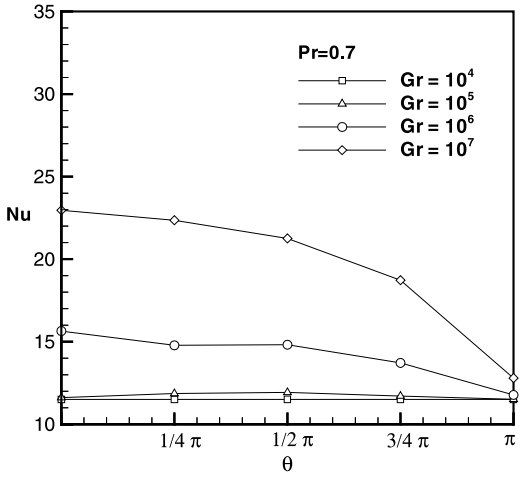

Fig. 8. Overall Nusselt number versus inclination angle at various Grashof numbers.

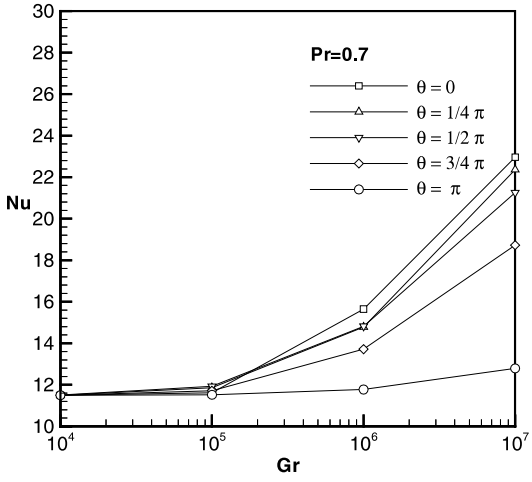

Fig. 9. Overall Nusselt number versus Grashof number at various inclination angles.

weaker convection with the thermal stratification observed in Figs. 6 and 7. As the thermal stratification prevails in the enclosure, the heat transfer between the two walls is dominated by conduction, instead of convection. Results presented in Fig. 9 indicate that only when the Grashof number is higher than 10^5, the increase in natural convection heat transfer becomes appreciable. However, at $\theta = \pi$, no significant heat transfer increase can be found even though the value of Gr is elevated to 10^7. This is because the natural convection is no longer a dominant heat transfer mode at this inclination angle.

Based on the numerical results obtained in this study, a correlation formula expressing the dependence of Nu on θ and Gr is obtained as

$$Nu = a(\theta)Gr^{b(\theta)} \tag{13}$$

where

$$a(\theta) = 1/(0.5155 - 0.0277\theta^{2.3139})$$
$$b(\theta) = (0.1539 - 0.0471\theta)/(1 - 0.2729\theta - 0.00681\theta^2) \tag{14}$$

which is valid for air within $10^4 \leqslant Gr \leqslant 10^7$ and $0 \leqslant \theta \leqslant \pi$, with maximum 4.7% error in comparison with the numerical solutions. Fig. 10 displays the deviation of Nu predicted by Eq. (13) in comparison with the numerical results.

The profiles for the distribution of the local Nusselt number on the flat wall for various inclination angles are shown in Fig. 11. In this figure, the value of Gr is fixed at 10^6. It is expected that the profiles for $\theta = 0$ and π are symmetric with respect to $x/L = 0.5$, and the magnitude of the local Nusselt number is always lower for $\theta = \pi$ than for $\theta = 0$. This may be attributed to the thermal stratification developed in the enclosure at $\theta = \pi$, as stated earlier. As the enclosure is inclined with $1/4\pi \leqslant \theta \leqslant 3/4\pi$, the symmetric feature is no longer seen. The thermal boundary layer formed along the flat wall, which is observed in Fig. 5, makes the local Nussult number increase with x/L monotonically within $0.2 \leqslant x/L \leqslant 0.9$.

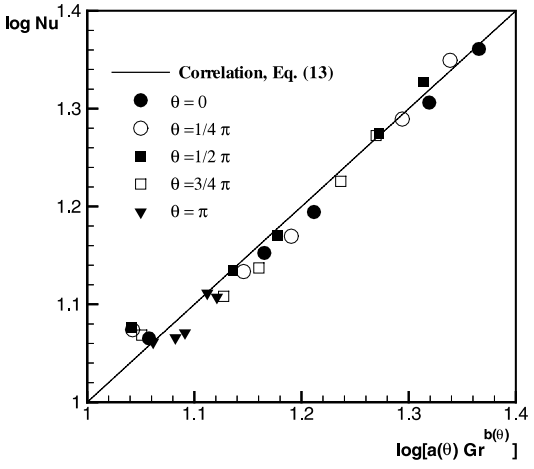

Fig. 10. Deviation of the correlation formula from the numerical results for overall Nusselt number.

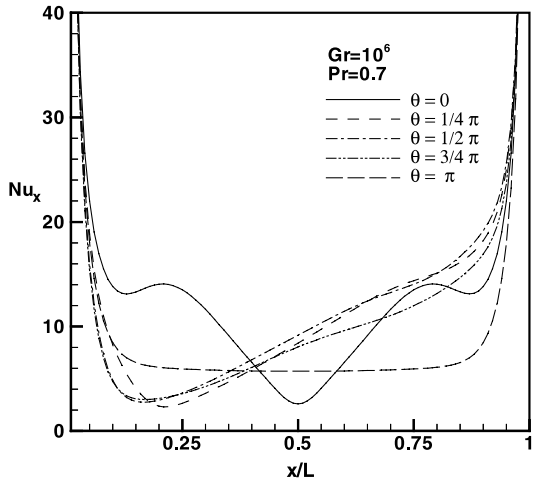

Fig. 11. Profiles of local Nusselt number at various inclination angles along the flat wall, at $Gr = 10^6$.

6. Concluding remarks

Numerical and experimental investigations are conducted to study the natural convective heat transfer and flow pattern in an inclined arc-shape enclosure. A flow-visualization technique using smoke is employed to observe the flow pattern, and a comparison between the numerical predictions and the visualized flow patterns has been made. In this study, Grashof number (Gr) is varied within the range $10^4 \leqslant Gr \leqslant 10^7$, and the inclination angle (θ) is in the range $0 \leqslant \theta \leqslant \pi$.

Results show that only when the Grashof number is higher than 10^5, the increase in natural convection heat transfer becomes appreciable. The vortex strength and pattern are found to be dependent on the inclination angle. At $\theta = 0$ or π, a flow pattern of two symmetric cells is found, whereas at other inclination angles the flow field features a one-cell pattern and a thermal boundary is formed along the flat wall. Comparison between the numerical solutions and the visualized flow patterns shows a good agreement.

Distributions of the local Nusselt number (Nu_x) on the flat wall for $\theta = 0$ and π are symmetric with respect to $x/L = 0.5$; however, the local Nusselt number is always lower for $\theta = \pi$ than for $\theta = 0$. As expected, overall Nusselt number (Nu) increases with Gr, and for the enclosure inclined at $\theta = \pi$, the magnitude of Nu attains a minimum value.

References

Ghia, U., Ghia, K.N., Shin, C.T., 1982. High-Re solutions for incompressible flow using the Navier–Stokes equations and a multigrid method. Journal of Computation Physics 48, 387–411.

Theodossiou, V.M., Sousa, A.C.M., 1986. An efficient algorithm for solving the incompressible fluid flow equations. International Journal for Numerical Methods in Fluids 6, 557–572.

Lee, J.H., Back, Y.R., Lee, S.R., Faghri, M., 1992. Natural convection in enclosures with an irregular wall. In: Reizes, J.A. (Ed.), Transport Phenomena in Heat and Mass Transfer. Elsevier, pp. 112–123.

Cheng, C.H., Chao, C.C., 1996. Numerical prediction of the buoyancy-driven flow in the annulus between horizontal eccentric elliptical cylinders. Numerical Heat Transfer Part A 30, 283–303.

Chang, M.H., Cheng, C.H., 1999. Predictions of lid-driven flow and heat convention in an arc-shape cavity. International Communications in Heat and Mass Transfer 26, 829–838.

Farouk Kothdiwala, A., Norton, B., Eames, P.C., 1995. The effect of variation of angle of inclination on the performance of low-concentration-ratio compound parabolic concentration solar collections. Solar Energy 55, 301–309.

Payver, P., 1991. Laminar heat transfer in the oil groove of a wet clutch. International Journal of Heat and Mass Transfer 34, 1791–1798.

Berger, E.J., Sadeghi, F., Krousgrill, C.M., 1996. Finite element modeling of engagment of rough and grooved wet clutches. Journal of Tribology 118, 137–146.

Khanafer, K.M., Chamkha, A.J., 1998. Hydromagnetic natural convention from an inclined porous square enclosure with heat generation. Numerical Heat Transfer Part A 33, 891–910.

Lai, J.C.S., Lu, D., 1996. Effect of wall inclination on the mean flow and turbulence characteristics in a two-dimensional wall jet. International Journal of Heat and Fluid Flow 17, 377–385.

Hartley, L.E., Martinez-Lozano, J.A., Utrillas, M.P., Tena, F., Pedros, R., 1999. The optimization of the angle of inclination of a solar collector to maximize the incident solar radiation. Renewable Energy 17, 291–309.

Cheng, C.H., Yu, J.H., 1999. Conjugate heat transfer in an inclined slab with an array of horizontal circular channels. Numerical Heat Transfer Part A 35, 779–796.

Cheng, C.H., Chen, H.N., Aung, W., 1997. Experimental study of the effect of transverse oscillation on convection heat transfer from a circular cylinder. Journal of Heat Transfer 119, 474–482.